



# Spectral Diagnostics of Solar Photospheric Bright Points

Q. Hao<sup>1,2</sup> , C. Fang<sup>1,2</sup>, M. D. Ding<sup>1,2</sup> , Z. Li<sup>1,2</sup>, and Wenda Cao<sup>3,4</sup> <sup>1</sup> School of Astronomy and Space Science, Nanjing University, Nanjing 210023, People's Republic of China; [fangc@nju.edu.cn](mailto:fangc@nju.edu.cn), [haoqi@nju.edu.cn](mailto:haoqi@nju.edu.cn)<sup>2</sup> Key Laboratory of Modern Astronomy and Astrophysics (Nanjing University), Ministry of Education, People's Republic of China<sup>3</sup> Big Bear Solar Observatory, New Jersey Institute of Technology, 40386 North Shore Lane, Big Bear City, CA 92314, USA<sup>4</sup> Center for Solar-Terrestrial Research, New Jersey Institute of Technology, University Heights, Newark, NJ 07102, USA

Received 2020 March 29; revised 2020 July 2; accepted 2020 July 14; published 2020 September 8

## Abstract

Through the use of the high-resolution spectral data and the broadband imaging obtained with the Goode Solar Telescope at the Big Bear Solar Observatory on 2013 June 6, the spectra of three typical photospheric bright points (PBP) have been analyzed. Based on the  $H\alpha$  and Ca II 8542 Å line profiles, as well as the TiO continuum emission, for the first time, the non-LTE semiempirical atmospheric models for the PBP are computed. The attractive characteristic is the temperature enhancement in the lower photosphere. The temperature enhancement is about 200–500 K at the same column mass density as in the atmospheric model of the quiet-Sun. The total excess radiative energy of a typical PBP is estimated to be  $1 \times 10^{27}$ – $2 \times 10^{27}$  erg, which can be regarded as the lower limit energy of the PBP. The radiation flux in the visible continuum for the PBP is about  $5.5 \times 10^{10}$  erg cm<sup>-2</sup> s<sup>-1</sup>. Our result also indicates that the temperature in the atmosphere above PBP is close to that of a plage. It gives clear evidence that PBP may contribute significantly to the heating of the plage atmosphere. Using our semiempirical atmospheric models, we estimate self-consistently the average magnetic flux density  $B$  in the PBP. It is shown that the maximum value is about 1 kG, and it decreases toward both higher and lower layers, reminding us of the structure of a flux tube between photospheric granules.

*Unified Astronomy Thesaurus concepts:* [Solar photosphere \(1518\)](#); [Solar atmosphere \(1477\)](#); [Solar chromosphere \(1479\)](#)

## 1. Introduction

Photospheric bright points (PBP) are small bright features observed in the photosphere. They exhibit bright emission in the visible continuum, such as the  $G$ -band and TiO band, or in the far wings of some spectral lines, such as  $H\alpha$  and Ca II H/K lines. Generally, PBP appear in the intergranular lanes and correspond to strong magnetic flux concentrations (Spruit 1976; Schuessler & Solanki 1988; Solanki 1993; Steiner et al. 2001; Steiner 2007; Riethmüller et al. 2014). Thus, the study of the physical characteristics of PBP, especially their temperature and density stratifications, can help us understand the properties and physical mechanisms occurring in small strong magnetic flux concentration, which may in turn reveal a possible source of coronal heating (Withbroe & Noyes 1977; Srivastava et al. 2017).

PBP have been studied since the 1970s. It was found that the PBP are best shown at  $H\alpha+2$  Å, and in the continuum images taken at 6439 Å (Dunn & Zirker 1973). In the images taken with the broadband filters at Ca II K and  $H\alpha$  bands, PBP occur singly or appear in chains or “crinkles,” lying in the intergranular lanes (Mehlretter 1974). Since then, several observations of PBP have been reported in the literature, together with theoretical models based on the concept of the flux tube (e.g., Spruit 1976; Schuessler & Solanki 1988; Steiner 2007). Similarly, semiempirical models based on observations of Stokes  $I$  and/or  $V$  profiles, as well as continuum contrasts (especially center-to-limb variation) have been put forward (Solanki 1993; Lagg et al. 2010; Cristaldi & Ermolli 2017). Most of them are filling factor dependent and are derived assuming Local Thermodynamic Equilibrium (LTE; see Solanki 1993; Steiner 2007 for review).

Later on, many authors used  $G$ -band images, combined with the broadband  $H\alpha$  and/or Ca II (H, K) imaging observations (Berger et al. 1995, 1998; Berger & Title 1996; Manso Sainz et al. 2011; Chitta et al. 2012; Xiong et al. 2017), while some authors used the broadband imaging at TiO 7057 Å (Cao et al. 2010; Liu et al. 2014, 2018) to study PBP. Recently, owing to the development of adaptive optics and image processing technology, high spatial resolution observations have been used to explore the characteristics of PBP in detail. For example, a 3D track-while-detect method was used to detect and track 27,696 PBP in the images of the  $G$ -band and the Ca II H line from SOT/Hinode (Xiong et al. 2017). A new algorithm was also developed to identify and track 2010 PBP in TiO 7057 Å images observed by the New Vacuum Solar Telescope of the Yunnan Observatory (Liu et al. 2018). They classified PBP into isolated (individual) and nonisolated (multiple PBP displaying splitting and merging behaviors) sets. Based on statistical studies and detailed analysis of individual cases, a series of characteristics of PBP have been obtained. That is, the diameters of PBP range from 150 to 400 km (Berger et al. 1995; Xiong et al. 2017; Liu et al. 2018); the lifetimes of PBP are about 200–1000 s or more (Muller & Keil 1983; de Wijn et al. 2005; Jafarzadeh et al. 2013; Keys et al. 2014; Xiong et al. 2017; Liu et al. 2018), and the brightness varies from 0.8 to 1.8 times the average background intensity (Mehlretter 1974; Berger et al. 1995; Liu et al. 2018). PBP show random-walk characteristics, with an average speed of 0.5–3 km s<sup>-1</sup> (Berger & Title 1996; Nisenson et al. 2003; Chitta et al. 2012; Criscuoli et al. 2012; Keys et al. 2014). As several authors indicated, the physical properties deduced from observations highly depend on the resolution of the observations (see, e.g., Spruit & Zwaan 1981; Knoelker et al. 1988; Criscuoli & Rast 2009), while so far the high-spectral resolution observations of PBP in both  $H\alpha$  and Ca II 8542 Å lines are rare. It is expected that high-spectral and

**Table 1**  
Characteristics of the PBPs

No.	Time (UT)	$C_H$	$C_{Ca}$	$C_{TiO}$	Lifetime (s)	Size ( $x \times y$ ) (arcsec)	$E$ (erg)	$F$ (erg $\text{cm}^{-2} \text{s}^{-1}$ )
1	17:03:04	0.089	0.075	0.079	437	$0.64 \times 0.48$	$1.46 \times 10^{27}$	$5.64 \times 10^{10}$
2	17:25:18	0.074	0.063	0.054	419	$0.64 \times 0.58$	$1.35 \times 10^{27}$	$5.55 \times 10^{10}$
3	17:28:05	0.091	0.090	0.085	503	$0.64 \times 0.54$	$2.03 \times 10^{27}$	$5.67 \times 10^{10}$

high spatial resolution observations and a detailed analysis will be made.

In this paper, we analyze the spectra of  $H\alpha$  and  $\text{Ca II } 8542 \text{ \AA}$  lines and the broadband TiO images of three typical PBPs, which were observed with the 1.6 m Goode Solar Telescope (GST; Cao et al. 2010; Goode & Cao 2012) at Big Bear Solar Observatory (BBSO). These spectral and imaging data were obtained simultaneously with high spatial resolution, which allows us to investigate the characteristics of the PBPs and construct non-LTE semiempirical models. We describe the observations in Section 2. The characteristics of the PBPs are described in Section 3. The non-LTE semiempirical models and the radiative energy estimation of the PBPs are given in Section 4. The estimation of the average magnetic flux density in the PBPs is given in Section 5. A discussion and summary are given in Section 6.

## 2. Observations

Using the Fast Imaging Solar Spectrograph (FISS; Chae et al. 2013) of GST/BBSO, we made spectral observations of the active region NOAA 11765 (N09E10) near the center of the solar disk from 16:50 UT to 19:00 UT on 2013 June 6. FISS is a dual-band echelle spectrograph, with two cameras, one for the  $H\alpha$  band with  $512 \times 256$  effective pixels, and the other for the  $\text{Ca II } 8542 \text{ \AA}$  band with  $502 \times 250$  effective pixels. Through a fast scanning of the slit, high-resolution 2D imaging spectra at the two bands can be obtained simultaneously. Each scan covered 150 steps with a spacing of  $0''.16$  and lasted about 30 s. The dispersions for the  $H\alpha$  and  $\text{Ca II } 8542 \text{ \AA}$  lines are  $0.019 \text{ \AA pixel}^{-1}$  and  $0.026 \text{ \AA pixel}^{-1}$ , respectively. The spatial sampling along the slit was  $0''.16 \text{ pixel}^{-1}$ . The field of view (FOV) of each scan is about  $40'' \times 25''$ . The exposure times were 30 ms and 60 ms for  $H\alpha$  and  $\text{Ca II } 8542 \text{ \AA}$  lines, respectively.

TiO images at  $7057 \text{ \AA}$  are recorded by the Broadband Filter Imager (BFI) with a cadence of 12–13 s. The filter bandpass of TiO  $7057 \text{ \AA}$  observation is  $10 \text{ \AA}$  and the typical exposure time is 0.8–1.5 ms. The FOV is  $70'' \times 70''$  and the pixel size is  $0''.034$ . Through the use of the speckle reconstruction algorithm, the TiO images with high spatial resolution were obtained. During the observations the seeing condition was better than  $1''$ . Through the use of a high-order adaptive optics (AO) systems AO-308, the diffraction limit was achieved in the observations.

## 3. Characteristics of the PBPs

By visual inspection of the FISS 2D spectra, three typical PBPs were detected during the observations. Table 1 lists some characteristics of the selected PBPs, including the time of the maximum intensity, lifetime, size, and energy. The contrasts of intensity,  $C = (I - I_0)/I_0$ , are also given in Table 1, where  $I$  and  $I_0$  are the average intensity of the PBPs and that of the background quiet-Sun at  $\pm(2-3) \text{ \AA}$  from the center of the  $H\alpha$  and  $\text{Ca II}$  lines, respectively.  $C_H$  and  $C_{Ca}$  are the contrasts for  $H\alpha$  and  $\text{Ca II}$  lines, respectively.  $C_{TiO}$  is the contrast at the TiO band. Due to the different resolutions between TiO and  $H\alpha$

data, the mean TiO intensity of the PBP is measured from a box of  $0''.7 \times 0''.7$  around the PBP, and the intensity of the quiet-Sun is averaged over a nearby box of  $3'' \times 3''$ . The lifetimes are obtained by counting the slit scanning steps during which the PBP appears. The size in the  $x$ -direction is estimated by counting the number of pixels along the scanning direction that the PBP occupies. The size in the  $y$ -direction is an average of the FWHM of the brightness distribution at  $\pm(2-3) \text{ \AA}$  from the center of the  $H\alpha$  line.

From Table 1, it can be seen that the PBPs have sizes of subarcseconds, generally less than  $0''.7$ . The lifetime of PBPs is less than 503 s, more or less similar to that of the photospheric granules. The contrasts of PBPs are within 0.054–0.091, not obviously varying in the observed wavelengths.

The TiO data were first destretched to remove the residual atmospheric seeing effects. Then we aligned the  $H\alpha$  wing ( $-1 \text{ \AA}$ ) images from the 2D spectra with the TiO images through the following steps. First, the TiO image was degraded to the same pixel-scale of the  $H\alpha$  image. Second, we set the  $H\alpha$  image as the reference image and calculate the correlation coefficients and offsets between the two images by tracing the characteristic features (e.g., sunspot umbra and penumbra regions). Next, the degraded TiO image was shifted according to the offsets to gain the largest correlation coefficient. We then recalculated the new offsets and correlation coefficients. This process was repeated until the offsets became stable and the correlation coefficient reached a relative maximum. Finally, the offsets were used to align and recover the original TiO images. After this process, the two kinds of data are rigidly aligned and the estimated alignment error is about  $0''.2$ . Through a careful coalignment of images at different wavelengths, it is found that the positions of the PBPs in  $H\alpha$  and  $\text{Ca II } 8542 \text{ \AA}$  bands correspond to the bright points in the TiO images. Figure 1 shows the locations of the three PBPs on the 2D  $H\alpha$  and TiO images. The red, yellow, and blue arrows (rectangles) indicate the positions of No.1, No.2, and No.3 PBPs, respectively (Figures 1(a), (b)). We found a close spatial correspondence between the  $H\alpha$  and TiO bright points, indicated by the corresponding arrows (Figures 1(c)–(d)).

Figure 2 shows the  $H\alpha$  and  $\text{Ca II } 8542 \text{ \AA}$  spectra and line profiles for the No.3 PBP. The profiles of the nearby quiet-Sun region are also shown for comparison. The intensity calibration was made by comparing our spectra compensated for the limb darkening with the disk center spectra given in Cox (2000). We took the intensity at the far wings of the lines as the continuum one. Though it is an approximate value, it does not significantly affect the contrast value, which is obtained by the ratio of the far wing intensities of the PBPs to that of the quiet-Sun. The continuum emission of the PBPs implies a significant temperature enhancement in the photosphere, compared to the quiet-Sun region. This is quite different from typical Ellerman bombs (EBs; for example, see No.2 EB in a previous study by Li et al. 2015), which have two emission bumps near  $\pm 1.0 \text{ \AA}$  of the  $H\alpha$  line and near  $\pm 0.6 \text{ \AA}$  of the  $\text{Ca II } 8542 \text{ \AA}$  line. This implies that PBPs and EBs are of different origins in the solar atmosphere (see also

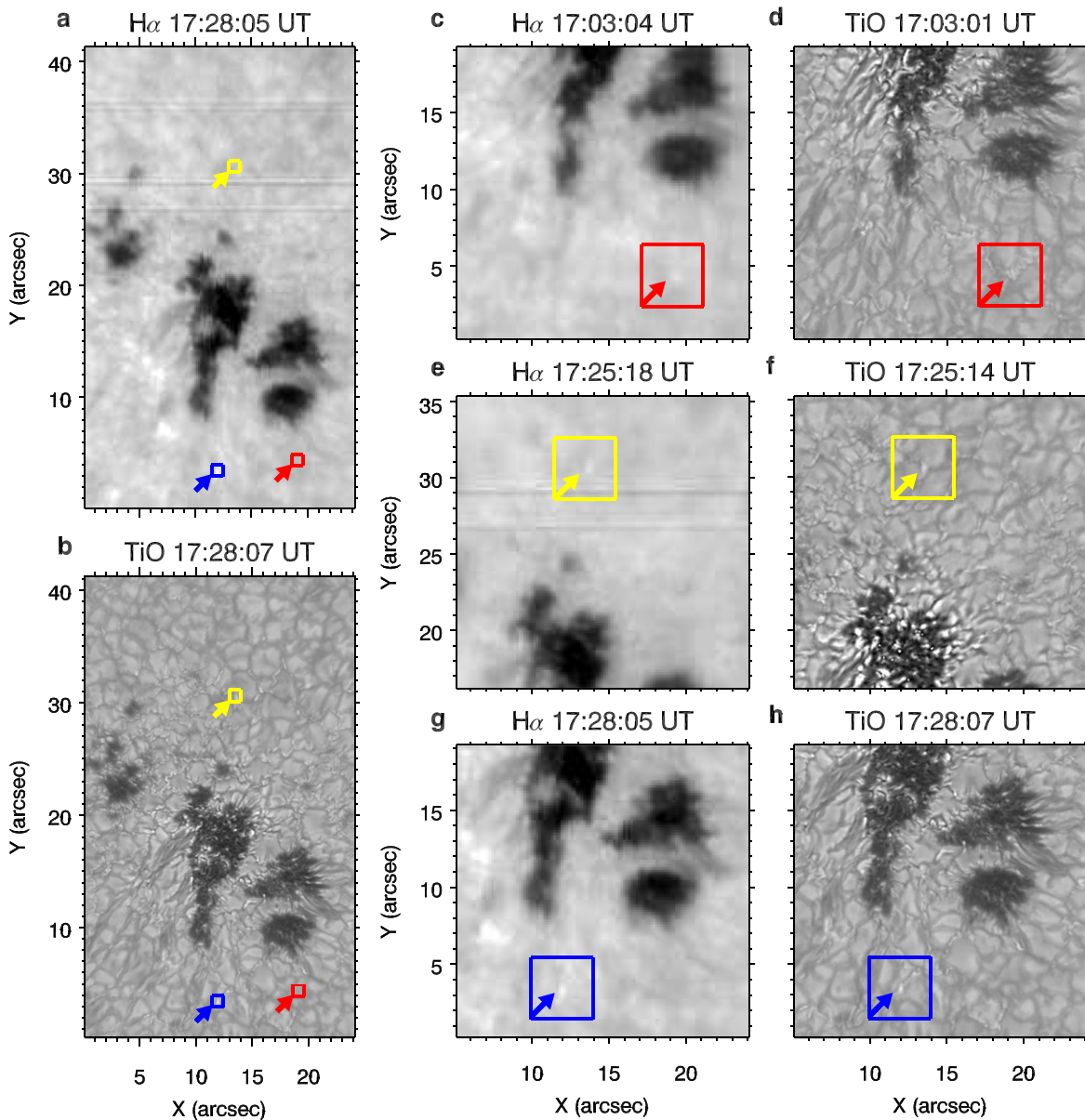


**Figure 1.** Three PBPs observed in  $H\alpha$  wing ( $-1 \text{ \AA}$ ) and TiO images. The red, yellow, and blue arrows and rectangles in (a) and (b) indicate the positions of No.1, No.2, and No.3 PBPs, respectively. (c)–(d) Zoomed-in  $H\alpha$  and TiO images showing the No.1 PBP. (e)–(f) Similar to (c)–(d), but for No.2 PBP. (g)–(h) Similar to (c)–(d), but for No.3 PBP.

Rutten et al. 2013 for a review). We adopt non-LTE semiempirical models to investigate thermal and magnetic properties of the PBPs in Section 4.

Figure 3 depicts temporal variations of relative intensity of the three PBPs. The relative intensity of each PBP at each time was measured as a mean value of  $(I - I_0)/I_{\max}$  at  $(-2.5 \text{ to } -3) \text{ \AA}$  from the center of the  $H\alpha$  core, where  $I_{\max}$  is the maximum intensity of the PBP. Figure 3 indicates that the intensity variation of PBPs is gradual, which gives a constraint on the modeling of PBPs, and its cause needs to be explored further.

#### 4. Non-LTE Semiempirical Modeling of the PBPs

##### 4.1. Computations of Non-LTE Semiempirical Atmospheric Models

Using both  $H\alpha$  and  $\text{Ca II } 8542 \text{ \AA}$  line profiles, combined with the continuum emission at the TiO band, we can compute the

semiempirical atmospheric models of the selected PBPs. It is well known that these lines are formed in a wide range of solar atmosphere, i.e., from the photosphere to the chromosphere (e.g., Vernazza et al. 1981). Thus, by fitting the observational line profiles and the TiO continuum, our semiempirical models can give the stratifications of physical quantities, such as temperature and density, etc., not only for the photosphere, but also for the chromosphere. Here we use a non-LTE computation method similar to the one described in Fang et al. (2006), with an additional constraint on the contrasts in the three wavebands. We used a four-level plus continuum and a five-level plus continuum atomic model for hydrogen and calcium, respectively. Generally speaking, given a tentative temperature stratification, we solved the statistical equilibrium equation, the radiative transfer equation, the hydrostatic equilibrium, and the particle conservation equations iteratively until the computed  $H\alpha$ ,  $\text{Ca II } 8542 \text{ \AA}$  line profiles and the contrasts in the three

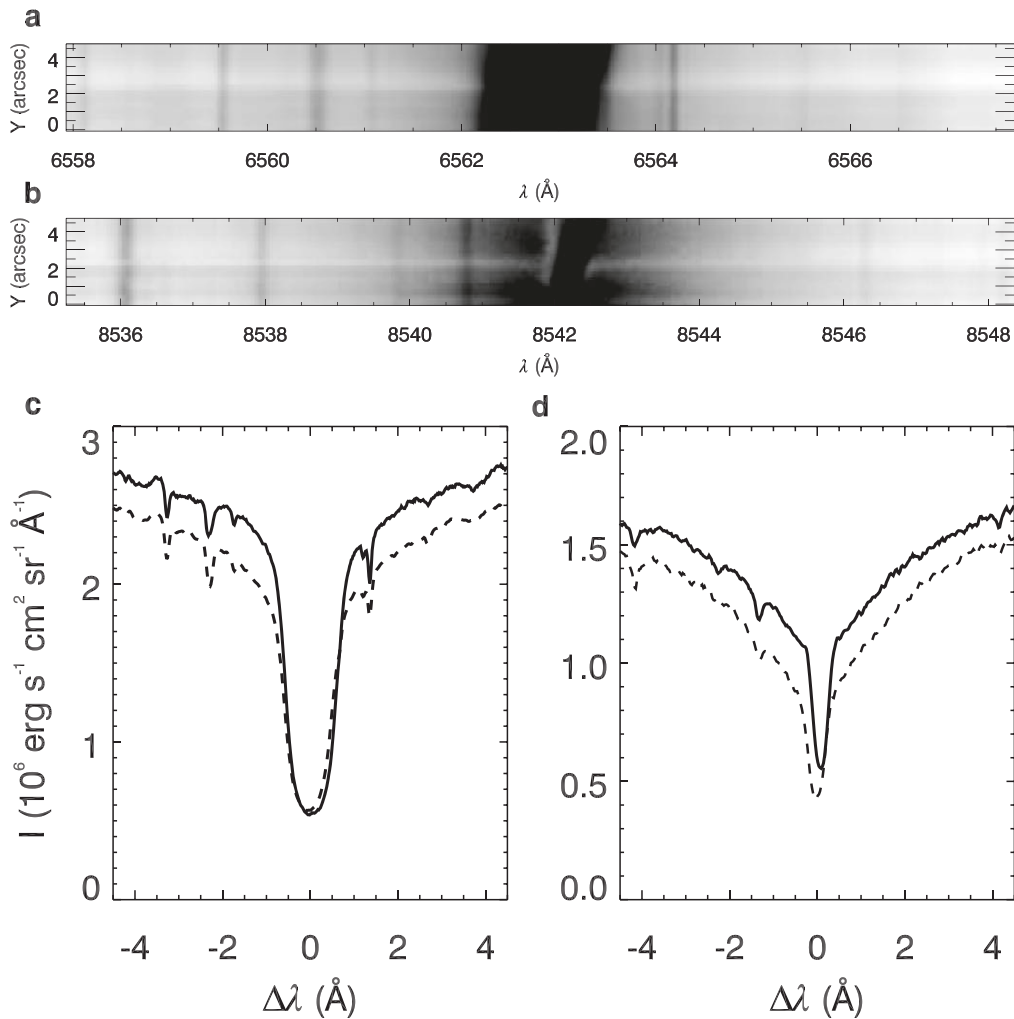


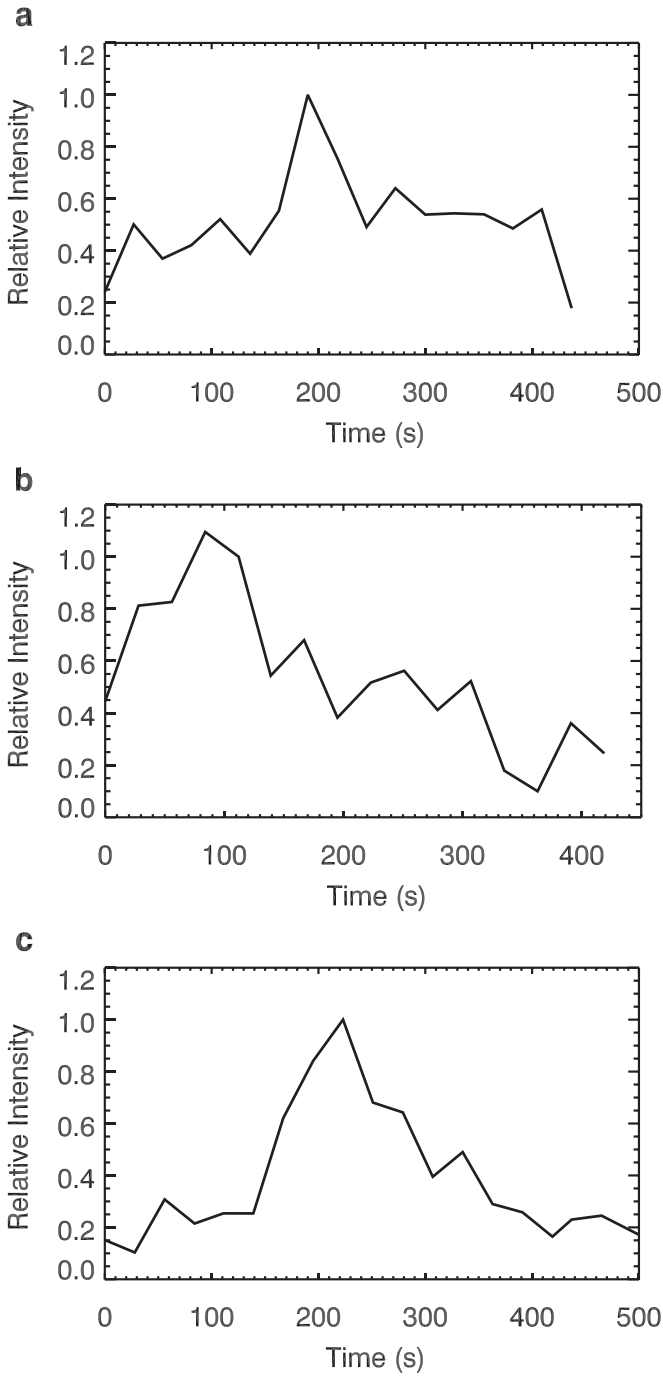
**Figure 2.** Observed spectra and line profiles of the No.3 PBP. (a)  $H\alpha$  spectrum. (b) Ca II 8542 Å spectrum. (c)  $H\alpha$  line profiles. (d) Ca II 8542 Å line profiles. The line profiles for the PBP are plotted as solid lines, while the line profiles at the nearby quiet-Sun are shown as dashed lines for comparison.

wavebands could be well matched. The computed continuum contrasts are obtained from the formula  $C = (I - I_0)/I_0$ , where the synthetic continuum intensity  $I$  of the PBPs is computed from our semiempirical models, and  $I_0$  is obtained from the quiet-Sun model (VALC; Vernazza et al. 1981) by using the same code. Both continuum intensities cover a wide wavelength range, from 3450 to 11000 Å. Indeed, it is better to use the magnetohydrostatic equilibrium equation if there is magnetic field in the flux tubes (PBPs). Since the analyzed PBPs are near the center of the solar disk and the computation is one-dimensional (1D) along the central axis of the flux tube, the hydrostatic equilibrium can still be used as an approximation. Since the convergence is considered achieved when the relative intensity error between the two iterations is less than  $10^{-7}$  and  $10^{-8}$  for hydrogen and calcium, respectively, a large number of iterations has been performed to achieve it.

The models can reproduce both the observed  $H\alpha$  and Ca II 8542 Å line profiles, as well as the contrasts in the three wavebands. Figure 4 gives the temperature stratifications of the atmospheric models of the three PBPs. For comparison, the temperature stratifications for the quiet-Sun model (VALC) and the semiempirical plage model (P; Fang et al. 2001) are also shown in Figure 4. Figure 5 depicts both the observed and computed line profiles of the No.3 PBP. In the computation, the

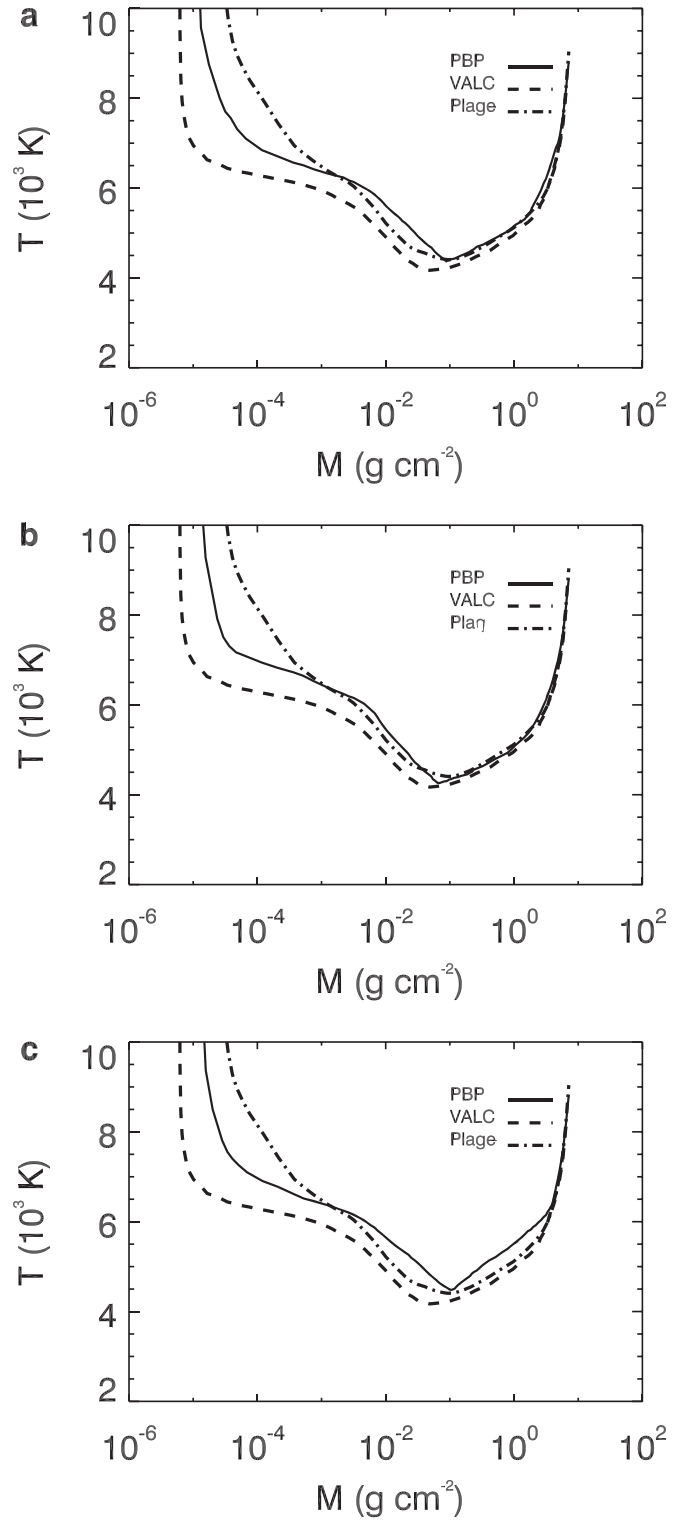
microturbulence velocity was taken as the same as that in the quiet-Sun model. A Gaussian macroturbulence velocity of  $5 \text{ km s}^{-1}$  is adopted to convolve the computed line profiles. The fitting of the contrasts in the three wavebands is provided in Figure 6. The contrast in the TiO band depends on the spatial resolution. In fact, if we take a box of  $0''.5 \times 0''.5$  around the PBP, the contrast would be 0.11, as shown in Figure 6. Moreover, the shape of PBP shows an irregular structure leading to a measurement error. As a compromise, we think that the fitting is acceptable. According to the noise (fluctuation) in the line profile observations, the estimated error in the intensity measurement is less than  $\pm 2\%$ . Considering the approximation of continuum intensity measurement at the far wings of the spectral lines, we take  $\pm 4\%$  as the total error bar for the two lines.

Figure 7 shows the temperature stratifications as a function of the optical depth at 5000 Å ( $\tau_{5000}$ ) for our model (PBP No.3) and several existing semiempirical models. Among them, Lagg2010 is the KG network model taken from Lagg et al. (2010), Crist2017 is a BPs model taken from Cristaldi & Ermolli (2017), and SP92 is a plage model taken from Solanki & Brigrlejev (1992). Lagg2010 was deduced from a high-resolution Stokes observation with the Fe I 5250.2 Å line and without introducing a magnetic filling factor. Crist2017 used spectropolarimetric data of the Fe I 6300 Å



**Figure 3.** Relative intensity variations of the three PBPs. (a), (b), and (c) correspond to No.1, No.2, and No.3 PBP, respectively. The start times for the PBPs are 16:59:54 UT, 17:23:54 UT, and 17:24:22 UT, respectively. The relative intensity of each PBP at each time was measured as a mean value of  $(I - I_Q)/I_{\max}$  at  $(-2.5$  to  $-3)$  Å from the center of the  $H\alpha$ , where the  $I_{\max}$  is the maximum intensity of the PBP.

line pair in small photospheric magnetic features. SP92 was deduced from Stokes  $I$  and  $V$  spectra of four C I and three Fe II lines. The calculation was performed by a line ratio technique in LTE. Bell2000 represents an internal model of a flux tube (Bellot Rubio et al. 2000). It used spatially averaged Stokes  $I$  and  $V$  spectra of the Fe I 6301.5 and 6302.5 lines, which were observed in a facular region. It can be seen that our model is consistent with SP92 and Crist2017 in the region of  $\log(\tau_{5000}) < 0$ , while the temperatures of Lagg2010 and Bell2000



**Figure 4.** Temperature stratifications derived for PBPs No.1 (a), No.2 (b), and No.3 (c) are shown as solid lines in the three panels. For comparison, the plage model described in Fang et al. (2001) is plotted by dashed-dotted lines, and the quiet-Sun model (VALC; Vernazza et al. 1981) is plotted by dashed lines in each panel.

are higher and lower than that of ours, respectively. Our model is consistent with the models of Lagg2010 and Crist2017 in the region of  $\log(\tau_{5000}) \geq 0$ , which is similar to the quiet-Sun model VALC, while the temperatures of Bell2000 and SP92 are higher and lower than that of ours, respectively. Note that all models

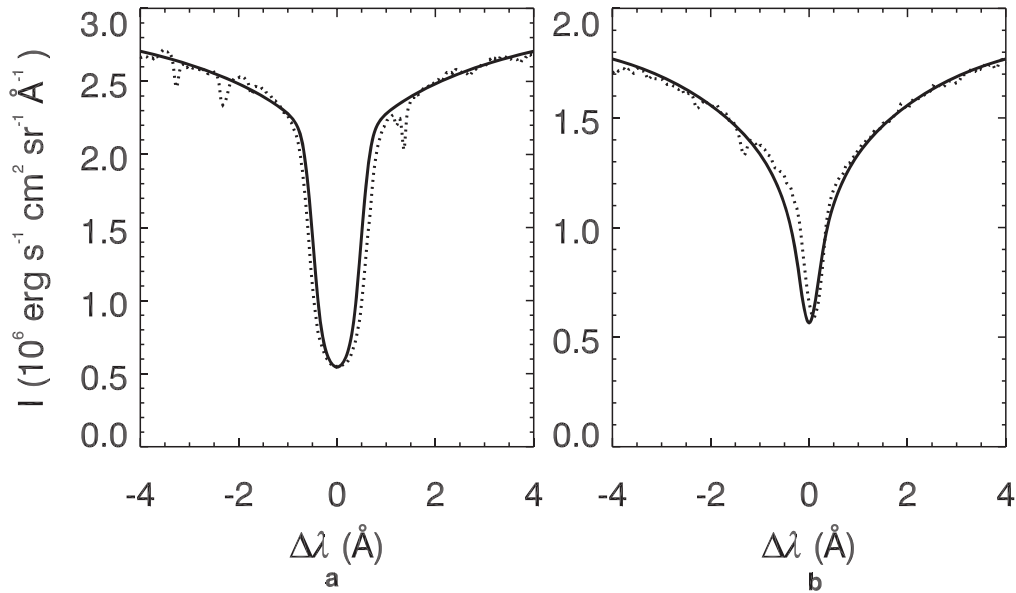


**Figure 5.** Comparison between the observed and computed line profiles. (a) The observed H $\alpha$  line profile for the No.3 PBP (dotted line) in comparison with the computed line profile from the semiempirical model (solid line). (b) Similar to panel (a) but for the Ca II 8542 Å line profiles. A Gaussian macroturbulence velocity of 5 km s $^{-1}$  is adopted to convolve the computed line profiles.

except for ours only account for the photosphere since they used photospheric lines exclusively to retrieve physical quantities.

Our non-LTE semiempirical models reveal significant temperature enhancement in the photosphere. The temperature enhancement is about 200–500 K, compared with the quiet-Sun model. The chromospheric temperature of the PBPs is higher than that of the quiet-Sun model, but comparable to the plage model presented in Fang et al. (2001). It may be caused by the enhanced radiation and/or some kinds of waves from the photosphere (e.g., Hasan et al. 2005). Thus, PBPs may be important contributors to the chromospheric heating, particularly to the heating of the plage.

According to our observed continuum contrasts and semiempirical models, the continuum spectra of all three PBPs show a rather flat wavelength dependence with a Balmer discontinuity in which the intensity at the red side of the Balmer limit (3646 Å) is larger than that at the blue side, contrary to the case of Type-I white-light flares (Hiei 1982). These characteristics are more or less similar to the Type-II white-light flares (Machado et al. 1986; Fang & Ding 1995), and the continuum emission comes mainly from negative hydrogen ions.

It is interesting to note that in our semiempirical models the chromospheric temperature enhancement begins at a deeper layer within PBPs than in the quiet-Sun. This result is consistent with previous results of small flux tube models (Solanki 1993; Hasan et al. 2005; Steiner 2007; Criscuoli & Rast 2009; Criscuoli et al. 2012).

#### 4.2. Radiative Energy Estimation of the PBPs

It is well known that the total radiative energy mainly comes from the continuum (e.g., Cox 2000; Fontenla et al. 2006), and thus we neglect the contribution from spectral lines. Using the semiempirical models and the computed continuum emission of the PBPs, we can estimate the total excess radiative energy  $E$

as follows:

$$E = \pi \frac{D}{2} S_{\text{PBP}} \int_{\lambda_1}^{\lambda_2} (I_{\lambda} - I_{Q\lambda}) d\lambda. \quad (1)$$

Considering that the relative intensity variations of PBPs are gradual, as shown in Figure 3, here we assume that the mean intensity during the lifetime ( $D$ ) of the PBP is about half of the measured peak intensity.  $S_{\text{PBP}}$  is the area of the PBP, which can be estimated by the PBP size ( $x \times y$ ) listed in Table 1.  $\lambda_1$  and  $\lambda_2$  are the lower and upper wavelength limits we have used in the integration of the continuum emission of the PBP. We take  $\lambda_1 = 4000$  Å and  $\lambda_2 = 10000$  Å.  $I_{\lambda}(0)$  and  $I_{Q\lambda}(0)$  are the intensity of the PBP and the quiet-Sun at the center of the solar disk, respectively. They can be estimated by using the following formula:

$$I_{\lambda}(0) = I_{\lambda}(\theta) / (1 - u_2 - v_2 + u_2 \cos \theta + v_2 \cos^2 \theta), \quad (2)$$

where  $I_{\lambda}(\theta)$  is the computed intensity and  $\theta$  is the heliocentric angle. In our case, the observed region is near the center of the solar disk with  $\cos \theta = 0.9722$ .  $u_2$  and  $v_2$  are the limb darkening coefficients, which can be taken from Cox (2000). We can also estimate the radiation flux  $F$  in continuum emission of the PBPs as follows:

$$F = \pi \int_{\lambda_1}^{\lambda_2} I_{\lambda}(0) d\lambda. \quad (3)$$

Using the Formulae (1)–(3), we have estimated the total excess radiative energies  $E$  and the radiation flux  $F$  of the three PBPs. The results are listed in Table 1. It can be seen that the total excess radiative energy for the PBPs is about  $1.4 \times 10^{27}$  to  $2 \times 10^{27}$  erg. The radiation flux  $F$  in the visible continuum of the PBPs is about  $5.5 \times 10^{10}$  erg cm $^{-2}$  s $^{-1}$ . There is no significant difference between the three PBPs.

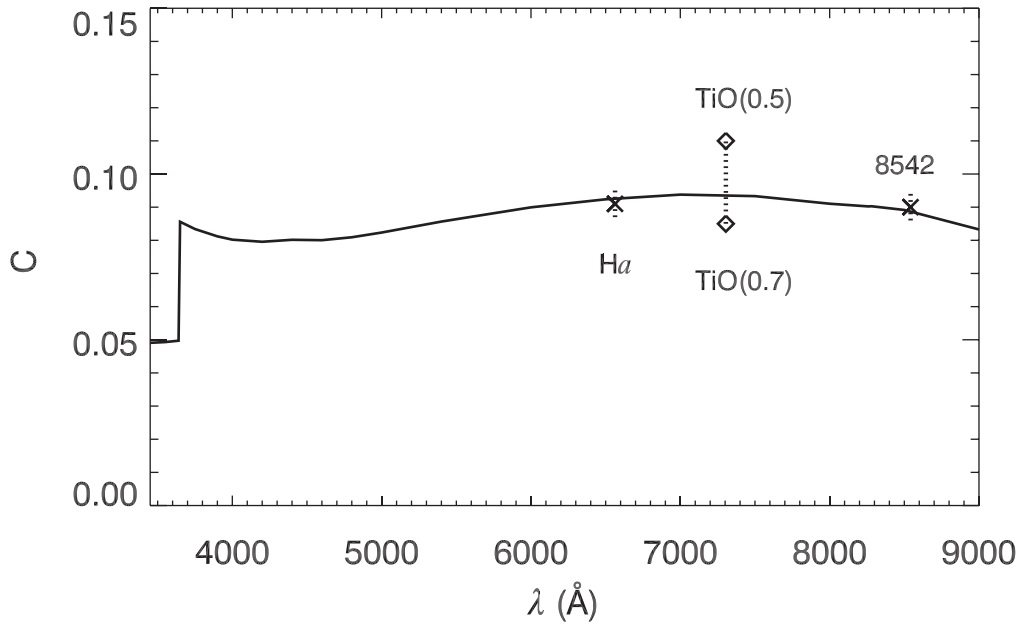


**Figure 6.** Fitting of the contrasts in the three wavebands of No.3 PBP. The crosses refer to observations of  $H\alpha$  and  $Ca II 8542 \text{ \AA}$  lines, the two rhombuses correspond to the values obtained from the TiO band in a box of  $0''.7 \times 0''.7$  and  $0''.5 \times 0''.5$  around the PBP, respectively, while the solid curve is the continuum emission computed from our semiempirical model.

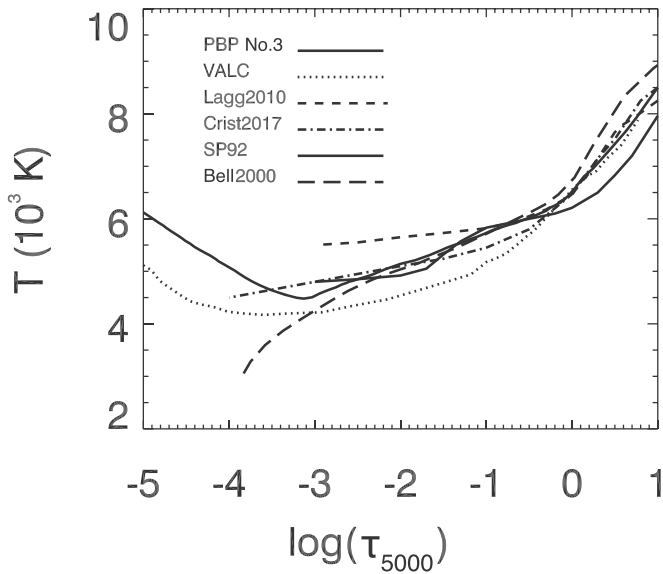


**Figure 7.** Temperature stratifications as a function of the optical depth at  $5000 \text{ \AA}$  for the semiempirical model of PBPs No.3 (solid line), Lagg2010 (dashed line), Crist2017 (dashed-dotted line), SB92 (dash three-dotted line), Bell2000 (long-dashed line), and VALC (dotted line). See the text for details.

A few estimations of PBP's radiative energy exist. However, our result can be compared with those from semiempirical models of solar active features. For example, Fontenla et al. (2006) give semiempirical models for different solar phenomena in the photosphere at moderate resolution. They estimated the radiation fluxes for plage and faculae to be  $4.21 \times 10^{10} \text{ erg cm}^{-2} \text{ s}^{-1}$  and  $4.17 \times 10^{10} \text{ erg cm}^{-2} \text{ s}^{-1}$  in the same wavelength interval as that of ours, respectively. Our estimation of the PBP's radiation flux is larger than that of Fontenla's. The difference may be due to the different spatial resolutions. It is interesting to note that the mean radiation flux of the solar disk is about  $2 \times 10^{10} \text{ erg cm}^{-2} \text{ s}^{-1}$  (Cox 2000), which is only 36% of the PBP's value.

## 5. Estimation of the Average Magnetic Flux Density in the PBPs

Several authors have pointed out that the Wilson depression occurring within magnetic flux tubes can explain the observed properties of PBPs (see, e.g., Solanki 1993; Shelyag et al. 2010; Rutten et al. 2013). That is, due to the strong magnetic field inside a thin flux tube, the horizontal pressure balance between the interior and external quiet-Sun atmosphere will cause a lower gas pressure inside the flux tube (Rutten et al. 2001; Vögler 2005; Riethmüller et al. 2014), which reduces the opacity so that the continuum radiation from the deeper layers with a higher temperature can escape and be observed. Up to now, unfortunately, due to the limited spatial resolution of magnetic observations, we cannot observe the flux tubes directly. However, several theoretical simulations and semiempirical modelings have been developed to interpret the physics of bright points (see, e.g., Solanki 1993; Steiner 2007; Lagg et al. 2010; Cristaldi & Ermolli 2017). From the point of view of observations, it is of importance to have a good knowledge of density and temperature stratifications inside the flux tubes. Fortunately, owing to advanced GST and its AO system, we can get the spectra of PBPs, which are manifestations of small flux tubes, with a very high spatial resolution. Using these observations, we computed the non-LTE semiempirical models of three PBPs without introducing a filling factor. Although the models are 1D, they provide estimates of the temperature and number density stratifications in the PBPs. Since the observed PBPs are near the center of the solar disk, we can consider that the stratifications are along the axis of small flux tubes. Thus, using the Wilson depression effect, we can self-consistently derive the average magnetic flux density in the flux tubes as follows.

Based on the assumption of a thin-tube model (Deinzer et al. 1984; Solanki & Brigljevic 1992), at a given height, there should be a horizontal pressure balance with the quiet-Sun

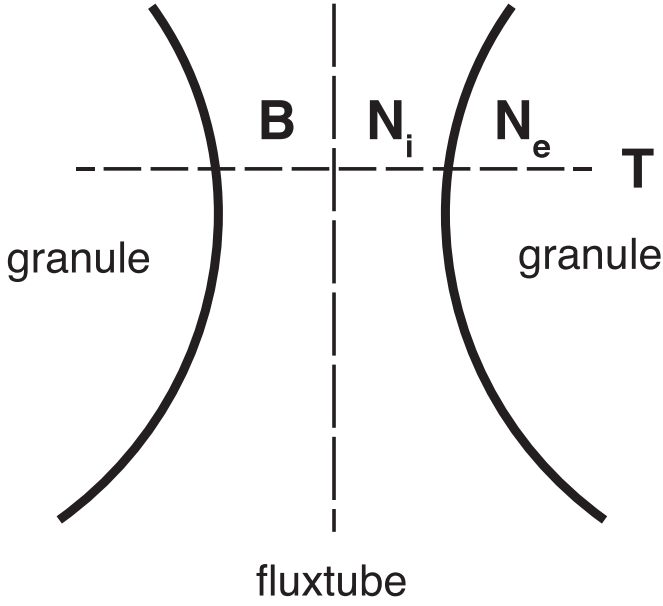


Figure 8. Schematic diagram of a flux tube between two granules.

atmosphere (see Figure 8). We have:

$$P_i + \frac{B^2}{8\pi} = P_e, \quad (4)$$

where  $B$  is the average magnetic flux density in the flux tube,  $P_{i,e}$  is the gas pressure insider or outside the flux tube. In this expression, the magnetic curvature terms are neglected, i.e., the force balance reduces to pressure balance, and the vertical and horizontal components of the pressure balance decouple from each other. For an ideal gas, the gas pressure can be expressed as

$$\begin{aligned} P &= NkT, \\ N &= (1 + A_{\text{He}})n_{\text{H}} + n_e, \end{aligned} \quad (5)$$

where  $n_{\text{H}}$  and  $n_e$  are the number density of hydrogen and electron, respectively.  $N$  is the total number density,  $A_{\text{He}}$  is the relative abundance of helium atoms. We adopted  $A_{\text{He}} = 0.1$ .  $k$  as the Boltzmann constant, and  $T$  as temperature, which should be the same in the internal and the external atmospheres at the same height because the radiative heat will exchange quickly. As our semiempirical models give the stratifications of temperature and all number densities  $N_i$ , we can get the average magnetic flux density  $B$  as

$$B = \sqrt{8\pi(N_e - N_i)kT}. \quad (6)$$

Figure 9 shows  $T$  versus  $N_i$  and  $N_e$ , which we got from the quiet-Sun model VALC, for No.1 and No.3 PBPs. The relationship for No.2 PBP is similar to that for No.1 PBP. It is clear that only in the lower photosphere  $N_e \geq N_i$ . This is consistent with the Wilson depression effect and we can get  $B$  from the Formula 6. Figure 10 depicts the results. It shows that the maximum value of  $B$  is approximately 1 kG, and it decreases toward both higher and lower layers, reminding us of the structure of a flux tube in the intergranular lanes between the photospheric granules, as illustrated in Figure 8. Note that the ‘‘real’’ value of  $B$  may be a bit higher than what we deduced, because the internal pressure in Formula 4 should be an

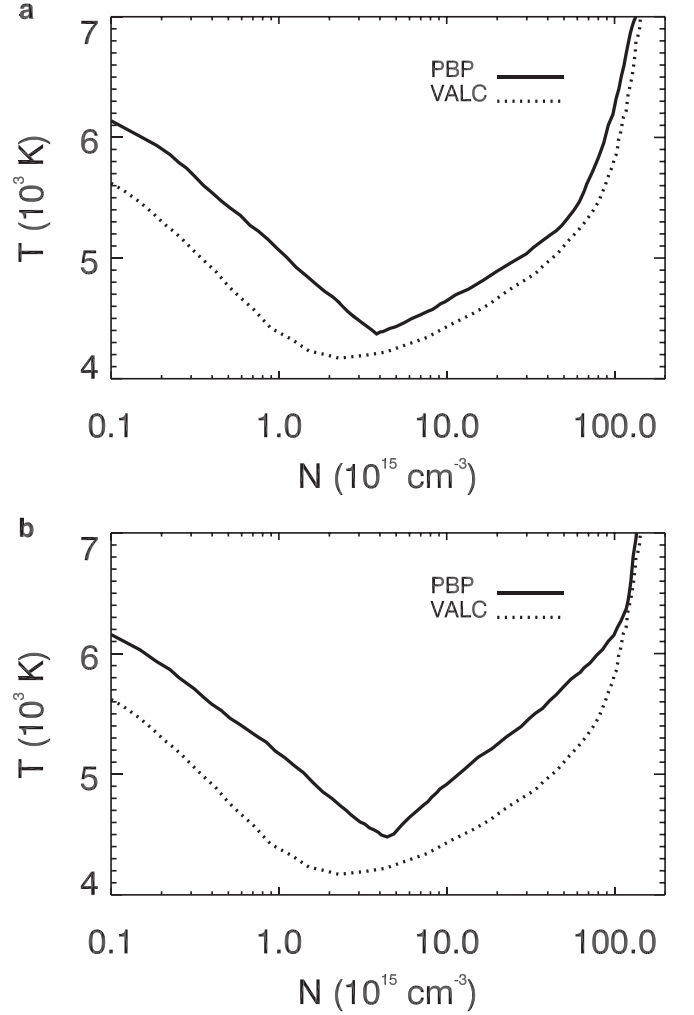


Figure 9.  $T$  vs.  $N_i$  and  $N_e$ , where  $N_i$  and  $N_e$  are the total number density in the internal and the external atmospheres of PBPs, respectively.  $N_i$  is taken from our semiempirical model, and  $N_e$  is taken from the quiet-Sun model of VALC. Panels (a) and (b) correspond to No.1 PBP and No.3 PBP, respectively.

average in the flux tube, which is less than the pressure at the flux tube center adopted from our semiempirical models.

However, the chromospheric temperature enhancement in the PBPs, as shown in Figure 4, cannot be explained by the Wilson depression effect, because in these layers  $N_e < N_i$ , as shown in Figure 9. This may be due to other mechanisms, such as MHD waves, radiation, and/or magnetic reconnection. It needs to be studied further.

## 6. Discussion and Conclusions

Using GST/BBSO FISS spectral data and BFI imaging, we have obtained the spectra of  $\text{H}\alpha$  and  $\text{Ca II } 8542 \text{ \AA}$  lines, and the  $\text{TiO } 7057 \text{ \AA}$  images for three selected PBPs. These spectral data and images were obtained simultaneously with high spatial resolution, which allow us to investigate the characteristics of the PBPs and construct non-LTE semiempirical models.

The attractive property of the PBP spectra is the continuum emission component at the two far wings of both  $\text{H}\alpha$  and  $\text{Ca II } 8542 \text{ \AA}$  lines (Figure 2), as well as the continuum emission at the  $\text{TiO}$  band. There is a one-to-one correspondence between the PBPs in the images at the two lines and the  $\text{TiO}$  bright

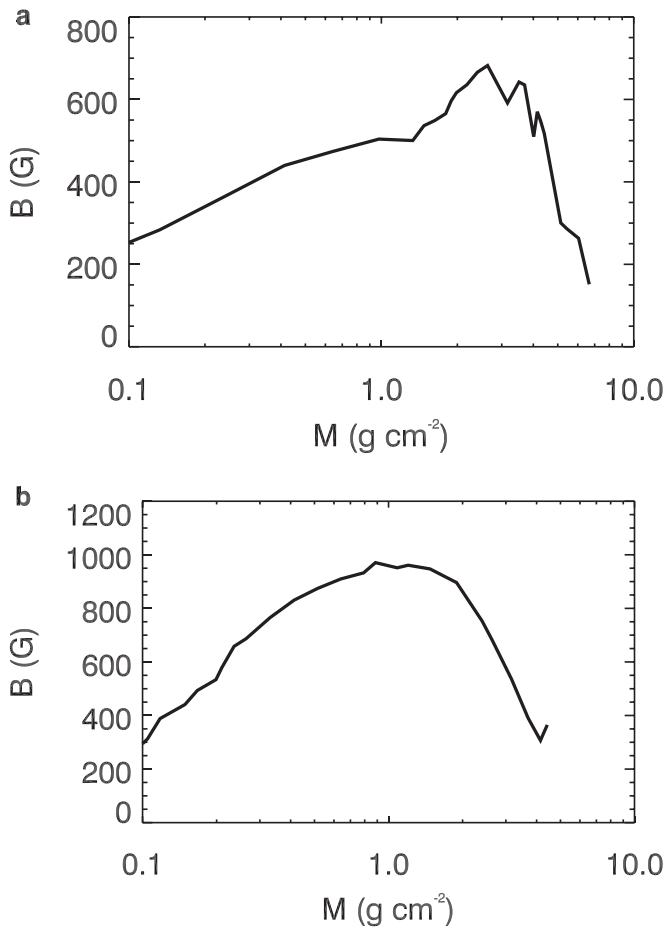


**Figure 10.** Estimation of the average magnetic flux density  $B$ . Panels (a) and (b) correspond to No.1 PBP and No.3 PBP, respectively.

points, both of which are located within the intergranular lanes between the photospheric granules (Figures 1(c)–(h)).

Using non-LTE theory, we have computed the semiempirical models for the three PBPs. Our results indicate that the temperature enhancement in the lower photosphere is about 200–500 K, compared with that in the quiet-Sun atmosphere at the same column mass density  $M$  (Figure 4). Through the use of the observed continuum emission, combined with our semiempirical models, the total excess radiative energy for the PBPs was estimated to be  $1 \times 10^{27}$ – $2 \times 10^{27}$  erg. The radiation flux  $F$  in the continuum emission of the PBPs is about  $5.5 \times 10^{10}$   $\text{erg cm}^{-2} \text{s}^{-1}$ .

Obviously, the total energy of PBPs should be larger than the radiative energy we estimated, because other energies, such as the magnetic and kinetic energy, are not included. If we assume that the extra energy, which can be transferred upward, is comparable to the radiative energy, then the total energy flux of PBPs can be estimated as follows. According to the statistics of PBPs, the number density of PBPs on the solar surface is about 0.25–0.97 PBPs  $\text{Mm}^{-2}$  (Sánchez Almeida et al. 2010; Keys et al. 2011; Feng et al. 2012; Liu et al. 2018). If we take 0.35 PBPs  $\text{Mm}^{-2}$  as the mean PBP density, and an extra energy of  $1 \times 10^{27}$  erg for one PBP, then the total energy density contributed by PBPs can be estimated as  $3.5 \times 10^{10}$   $\text{erg cm}^{-2}$ . If we take the lifetime of PBPs to be about 400 s, then the energy flux provided by PBPs approximates  $8.8 \times 10^7$   $\text{erg cm}^{-2} \text{s}^{-1}$ . Thus, it is reasonable to expect that the PBPs may contribute to

the heating of the solar upper atmosphere via waves (like the Alfvén wave), radiation, or other mechanisms.

Our non-LTE semiempirical modeling confirms that the temperature enhancement of PBPs in the lower photosphere could be explained by the Wilson depression within the flux tubes (e.g., Rutten et al. 2001; Vögler 2005; Riethmüller et al. 2014). Moreover, as PBPs manifest the small magnetic flux tubes, using our semiempirical models and under the thin-tube assumption, we derived the average magnetic flux density of the flux tubes to be one kilo-Gauss.

It should be mentioned that the temperature enhancement in the PBPs obtained in the chromosphere, as shown in Figure 4, cannot be explained by the Wilson depression effect. This may be due to the other mechanisms, such as MHD waves, radiation, and/or Joule heating. Since we do not have high-resolution magnetograms, this topic is beyond the scope of this paper.

We summarize the conclusions as follows:

1. The attractive characteristics of the PBP spectra are the continuum emission component at the far wings ( $\geq \pm 3 \text{ \AA}$ ) of both the  $\text{H}\alpha$  and  $\text{Ca II } 8542 \text{ \AA}$  lines, as well as in the continuum of the  $\text{TiO}$  band. Using the continuum measurements and our semiempirical modeling, we have estimated the radiative energy of the PBPs. Our results indicate that the total excess radiative energy of the PBPs is  $1 \times 10^{27}$ – $2 \times 10^{27}$  erg, and the radiation flux in the visible continuum of the PBPs is about  $5.5 \times 10^{10}$   $\text{erg cm}^{-2} \text{s}^{-1}$ . Our result reveals that the PBPs may more or less contribute to the heating of the solar upper atmosphere, in particular, to the heating of the plage.
2. The non-LTE semiempirical atmospheric models of the PBPs have been computed. The common characteristic is the temperature enhancement in the lower photosphere. The temperature enhancement is about 200–500 K. Our result also indicates that the temperature in the atmosphere above PBPs is close to the plage one. It gives clear evidence that the PBPs may contribute significantly to the heating of the plage atmosphere. Using these models, we estimate self-consistently the average magnetic flux density  $B$  in the PBPs. It is shown that the maximum value is about one kilo-Gauss, and it decreases toward both higher and lower layers, reminding us of the structure of flux tubes in the intergranular lanes between the photospheric granules.
3. We derived self-consistently the average magnetic flux density of the flux tubes to be one kilo-Gauss using our semiempirical models with the thin-tube assumption but without introducing a filling factor.

We thank the referee for a careful reading and constructive comments that helped to improve the paper. We would like to give our sincere gratitude to the staff at the Big Bear Solar Observatory (BBSO) of the New Jersey Institute of Technology (NJIT) for their enthusiastic help during C.F.’s stay there. This work has been supported by NSFC under grants 11533005, 11203014, 11025314, 11373023, 11729301, 11703012, 11733003, and Jiangsu NSF under grant BK20170619. Q.H. is also supported by the Fundamental Research Funds for the Central Universities under grant 14380032. BBSO operation is supported by NJIT and US NSF AGS-1821294 grant. GST operation is partly supported by the Korea Astronomy and Space Science Institute, the Seoul National University, the KLSA-CAS and the Operation,

Maintenance and Upgrading Fund of CAS for Astronomical Telescope and Facility Instruments.

### ORCID iDs

Q. Hao  <https://orcid.org/0000-0002-9264-6698>  
 M. D. Ding  <https://orcid.org/0000-0002-4978-4972>  
 Wenda Cao  <https://orcid.org/0000-0003-2427-6047>

### References

- Bellot Rubio, L. R., Ruiz Cobo, B., & Collados, M. 2000, *ApJ*, **535**, 489  
 Berger, T. E., Löfdahl, M. G., Shine, R. S., & Title, A. M. 1998, *ApJ*, **495**, 973  
 Berger, T. E., Schrijver, C. J., Shine, R. A., et al. 1995, *ApJ*, **454**, 531  
 Berger, T. E., & Title, A. M. 1996, *ApJ*, **463**, 365  
 Cao, W., Gorceix, N., Coulter, R., et al. 2010, *AN*, **331**, 636  
 Chae, J., Park, H.-M., Ahn, K., et al. 2013, *SoPh*, **288**, 1  
 Chitta, L. P., van Ballegoijen, A. A., Rouppe van der Voort, L., DeLuca, E. E., & Kariyappa, R. 2012, *ApJ*, **752**, 48  
 Cox, A. N. 2000, *Allen's Astrophysical Quantities* (New York: Springer)  
 Criscuolo, S., del Moro, D., Giorgi, F., et al. 2012, *MSAIS*, **19**, 93  
 Criscuolo, S., & Rast, M. P. 2009, *A&A*, **495**, 621  
 Cristaldi, A., & Ermolli, I. 2017, *ApJ*, **841**, 115  
 de Wijn, A. G., Rutten, R. J., Haverkamp, E. M. W. P., & Sütterlin, P. 2005, *A&A*, **441**, 1183  
 Deinzer, W., Hensler, G., Schuessler, M., & Weisshaar, E. 1984, *A&A*, **139**, 426  
 Dunn, R. B., & Zirker, J. B. 1973, *SoPh*, **33**, 281  
 Fang, C., & Ding, M. D. 1995, *A&AS*, **110**, 99  
 Fang, C., Ding, M. D., Hénoux, J. C., & Livingston, W. C. 2001, *ScChA*, **44**, 528  
 Fang, C., Tang, Y. H., Xu, Z., Ding, M. D., & Chen, P. F. 2006, *ApJ*, **643**, 1325  
 Feng, S., Ji, K.-f., Deng, H., Wang, F., & Fu, X.-d. 2012, *JKAS*, **45**, 167  
 Fontenla, J. M., Avrett, E., Thuillier, G., & Harder, J. 2006, *ApJ*, **639**, 441  
 Goode, P. R., & Cao, W. 2012, *Proc. SPIE*, **8444**, 844403  
 Hasan, S. S., van Ballegoijen, A. A., Kalkofen, W., & Steiner, O. 2005, *ApJ*, **631**, 1270  
 Hiei, E. 1982, *SoPh*, **80**, 113  
 Jafarzadeh, S., Solanki, S. K., Feller, A., et al. 2013, *A&A*, **549**, A116  
 Keys, P. H., Mathioudakis, M., Jess, D. B., Mackay, D. H., & Keenan, F. P. 2014, *A&A*, **566**, A99  
 Keys, P. H., Mathioudakis, M., Jess, D. B., et al. 2011, *ApJL*, **740**, L40  
 Knoelker, M., Schuessler, M., & Weisshaar, E. 1988, *A&A*, **194**, 257  
 Lagg, A., Solanki, S. K., Riethmüller, T. L., et al. 2010, *ApJL*, **723**, L164  
 Li, Z., Fang, C., Guo, Y., et al. 2015, *RAA*, **15**, 1513  
 Liu, Y., Xiang, Y., Erdélyi, R., et al. 2018, *ApJ*, **856**, 17  
 Liu, Z., Xu, J., Gu, B.-Z., et al. 2014, *RAA*, **14**, 705  
 Machado, M. E., Avrett, E. H., Falciani, R., et al. 1986, in *The Lower Atmosphere of Solar Flares*, ed. D. F. Neidig & M. E. Machado (Sunspot, NM: National Solar Observatory), 483  
 Manso Sainz, R., Martínez González, M. J., & Asensio Ramos, A. 2011, *A&A*, **531**, L9  
 Mehlretter, J. P. 1974, *SoPh*, **38**, 43  
 Muller, R., & Keil, S. L. 1983, *SoPh*, **87**, 243  
 Nissenon, P., van Ballegoijen, A. A., de Wijn, A. G., & Sütterlin, P. 2003, *ApJ*, **587**, 458  
 Riethmüller, T. L., Solanki, S. K., Berdyugina, S. V., et al. 2014, *A&A*, **568**, A13  
 Rutten, R. J., Kiselman, D., Rouppe van der Voort, L., & Plez, B. 2001, in *ASP Conf. Ser. 236, Advanced Solar Polarimetry—Theory, Observation, and Instrumentation*, ed. M. Sigwarth (San Francisco, CA: ASP), 445  
 Rutten, R. J., Vissers, G. J. M., Rouppe van der Voort, L. H. M., Sütterlin, P., & Vitas, N. 2013, *JPhCS*, **440**, 012007  
 Sánchez Almeida, J., Bonet, J. A., Vitičić, B., & del Moro, D. 2010, *ApJL*, **715**, L26  
 Schuessler, M., & Solanki, S. K. 1988, *A&A*, **192**, 338  
 Shelyag, S., Mathioudakis, M., Keenan, F. P., & Jess, D. B. 2010, *A&A*, **515**, A107  
 Solanki, S. K. 1993, *SSRv*, **63**, 1  
 Solanki, S. K., & Brigljevic, V. 1992, *A&A*, **262**, L29  
 Spruit, H. C. 1976, *SoPh*, **50**, 269  
 Spruit, H. C., & Zwaan, C. 1981, *SoPh*, **70**, 207  
 Srivastava, A. K., Shetye, J., Murawski, K., et al. 2017, *NatSR*, **7**, 43147  
 Steiner, O. 2007, in *Modern Solar Facilities—Advanced Solar Science*, ed. F. Kneer, K. G. Puschmann, & A. D. Wittmann (Göttingen: Universitätsverlag Göttingen), 321  
 Steiner, O., Hauschildt, P. H., & Bruls, J. 2001, *A&A*, **372**, L13  
 Vernazza, J. E., Avrett, E. H., & Loeser, R. 1981, *ApJS*, **45**, 635  
 Vögler, A. 2005, *MmSAI*, **76**, 842  
 Withbroe, G. L., & Noyes, R. W. 1977, *ARA&A*, **15**, 363  
 Xiong, J., Yang, Y., Jin, C., et al. 2017, *ApJ*, **851**, 42